AGU ADVANCING EARTH AND SPACE SCIENCE

JGR Solid Earth

Key Points:

- Uplift at Three Sisters was first observed in 1995–1996, accelerated during 1998–1999, peaked in rate in late 1999, and continues
- The most likely cause is magma intrusion about 5 km west of the summit of South Sister volcano, about 6 km below the surface
- Intrusion volume is 49×10^6 m^3 if crustal response is elastic, or 21×10^6 m^3, if the intrusion is surrounded by a viscoelastic shell

Supporting Information:

Supporting Information may be found in the online version of this article.

Correspondence to:

D. Dzurisin,
dzurisin@usgs.gov

Author Contributions:

Conceptualization: Michael Lisowski, Robert McCaffrey, Charles W. Wicks, Daniel Dzurisin
Data curation: Michael Lisowski, Charles W. Wicks, Daniel Dzurisin
Formal analysis: Michael Lisowski, Robert McCaffrey, Charles W. Wicks
Investigation: Michael Lisowski, Robert McCaffrey, Charles W. Wicks, Daniel Dzurisin
Methodology: Michael Lisowski, Robert McCaffrey, Charles W. Wicks, Daniel Dzurisin
Validation: Michael Lisowski, Robert McCaffrey

Geodetic Constraints on a 25-year Magmatic Inflation Episode Near Three Sisters, Central Oregon

Michael Lisowski[1] , Robert McCaffrey[2] , Charles W. Wicks[3] , and Daniel Dzurisin[1]

[1]U.S. Geological Survey, David A. Johnston Cascades Volcano Observatory (retired), Vancouver, WA, USA, [2]Department of Geology, Portland State University (retired), Portland, OR, USA, [3]U.S. Geological Survey, Moffett Field, CA, USA

Abstract Crustal inflation near the Three Sisters volcanic center documented since the mid-1990s has persisted for more than two decades. We update past analyses of the event through 2020 by simultaneously inverting InSAR interferograms, GPS time series, and leveling data for time-dependent volcanic deformation source parameters. We explore several source models to estimate how the deformation rate varied through time and to identify parameters that can reproduce measured deformation. Our preferred model is a Mogi source 4.1 km below sea level (5.9 km below the surface) about 5 km west of the summit of South Sister. Inflation started in late 1995 or 1996; the rate increased rapidly during 1998–1999, and peaked in late 1999, resulting in maximum surface uplift of about 30 cm by mid-2020. Since 2000, the inflation rate generally declined exponentially with a time constant of about 6 years. Two source inflation scenarios fit the data equally well. In the first, the crust surrounding the source is elastic and the net source-volume increase, which we attribute to persistent magma input, has been about 49×10^6 m^3. The second scenario adds a viscoelastic shell surrounding the Mogi source. In that case, an injection of about 21×10^6 m^3 of magma prior to 2000, followed by continuing relaxation of the viscoelastic shell, can account for most of the observed surface deformation. In both scenarios, modeling reveals quasiperiodic increases in the inflation rate (pulses) with a recurrence interval of 3–4 years, both before and after 2000.

Plain Language Summary Ground surface deformation is common in active volcanic areas and can be diagnostic of subsurface processes, including changes in magma storage that often presage eruptions. At the Three Sisters volcanic center in central Oregon, USA, uplift that was first observed in the mid-1990s is continuing (August 2021). Our study updates earlier analyses by modeling all available deformation datasets. The source is roughly spherical in shape and located about 5 km west of the summit of South Sister volcano, at a depth of about 6 km below the surface. Uplift started slowly in late 1995 or 1996, accelerated rapidly during 1998–1999, and the rate peaked in late 1999, resulting in maximum uplift of about 30 cm. Since 2000, the uplift rate has generally declined to a current value of about 3 mm/yr. Two scenarios fit the data equally well. In the first, the crust is elastic and the net volume increase, which we attribute to magma injection, has been about 49×10^6 m^3. The second scenario adds a viscoelastic shell surrounding the magma intrusion zone. In that case, an injection of about 21×10^6 m^3 of magma prior to 2000, followed by continuing relaxation of the viscoelastic shell, can account for the observed deformation.
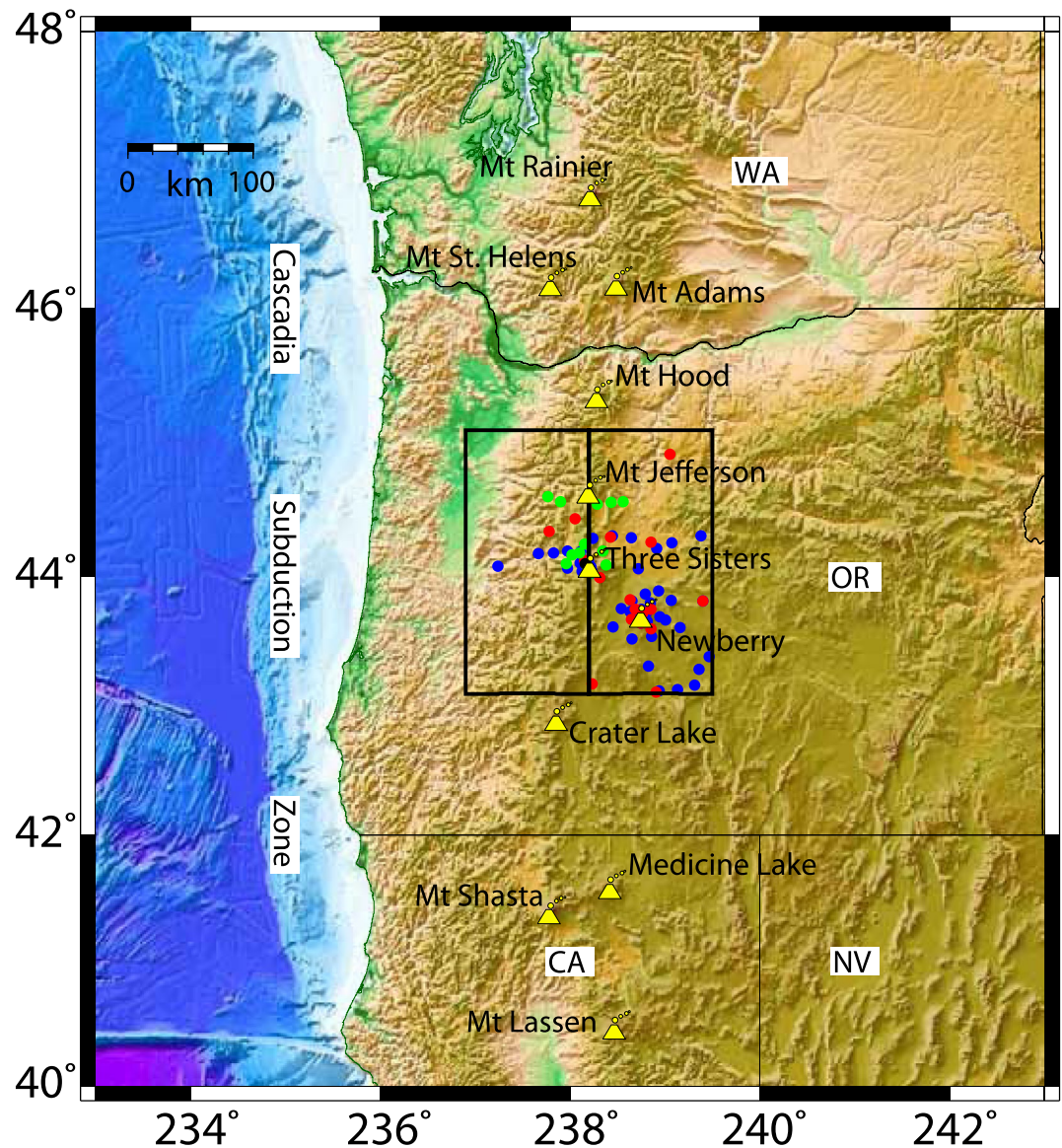
1. Introduction

The central Oregon portion of the Cascade volcanic arc comprises hundreds of mafic to silicic vents (Guffanti & Weaver, 1988) and has produced the highest Quaternary (2–0 Ma) extrusion rate along the entire arc, 3–6 km^3/km/m.y. (i.e., 3–6 cubic kilometers of material extruded per kilometer of arc length per million years) (Sherrod & Smith, 1990). Clustered near its center are North Sister, Middle Sister, South Sister, and Broken Top, large composite cones with an aggregate volume of 30–40 km^3 (Figure 1), together known as the Three Sisters. Mount Bachelor, a late-Pleistocene to Holocene stratovolcano about 11 km south of Broken Top, lies at the north end of the 25-km-long, north-south trending, Mount Bachelor volcanic chain, which is composed of numerous cinder cones, lava flows, and shield volcanoes. The Three Sisters are progressively younger from north to south; only South Sister has produced Holocene eruptions, most recently in two closely spaced episodes between 2.2 and 2.0 ka (Hildreth et al., 2012; Scott, 1987; Sherrod et al., 2004).

Starting in the mid-1990s, a circular area about 20 km in diameter that we call the Three Sisters Bulge (TSB), centered about 5 km west of South Sister, moved upward and outward, initially at rates up to several cm/yr.

Writing – original draft: Michael Lisowski, Robert McCaffrey, Charles W. Wicks, Daniel Dzurisin
Writing – review & editing: Michael Lisowski, Robert McCaffrey, Charles W. Wicks, Daniel Dzurisin

Figure 1. Map of the U.S. Pacific Northwest showing study area of the Three Sisters volcanic center. Yellow triangles mark major volcanoes along the arc. Blue dots mark locations of survey-mode GPS stations, green dots are semipermanent GPS, and red dots are continuous GPS stations. Two rectangles outline blocks used in the study.

Remarkably few earthquakes accompanied the ground deformation, which is continuing at a much-reduced rate in the present day. Previous studies (Dzurisin et al., 2006, 2009; Riddick & Schmidt, 2011; Rodríguez-Molina et al., 2021; Wicks et al., 2002) concluded that the bulge most likely results from intrusion of magma into the crust at a depth of 5–7 km. In this paper, we update the analysis with an additional decade of observations and, in the case of Rodríguez-Molina et al. (2021), by modeling a viscoelastic crustal response scenario. By our estimates, by mid-2020 the center of the bulge had increased by 30 cm in height, and it was continuing to rise at about 3 mm/yr.

Since its discovery by satellite interferometry (InSAR) in 2001 (Wicks et al., 2002), the TSB has been studied with a variety of geodetic techniques. InSAR tracked its early growth (Wicks et al., 2002). GPS, leveling, and InSAR measurements demonstrated that it continued to grow through 2004 (Dzurisin et al., 2006), and a follow-up study based only on GPS and leveling data showed that the deformation continued but its rate decayed exponentially during 2001–2008 (Dzurisin et al., 2009). Riddick and Schmidt (2011) updated InSAR

results through 2010 and constructed an InSAR time series that indicated slow growth of the TSB as early as 1996, and a larger growth rate starting in 1998 that slowed at the time of a small earthquake swarm in March 2004. Although the hypothesized inflection in the growth rate occurred after the May 2001 installation of a continuous GPS monitoring station (HUSB) in the deforming area, it is not obvious in the smoothly decaying station displacement time series reported by Dzurisin et al. (2009). Because piecewise linear and exponential decays indicate different source behaviors, we investigate this issue further here. The earlier studies that assumed elastic behavior of surrounding crust hypothesized a range of source geometries and depths to account for the observed deformation pattern, from deeper pressurized sills to shallower vertically elongate spheroids. There was general agreement that the surface inflation was consistent with a source volume increase of $50–65 \times 10^6$ m^3 through 2010. Rodríguez-Molina et al. (2021), in contrast, suggested the deformation since 2000 is a viscoelastic response to a much smaller injection event that ended in the late 1990s. We explore both alternatives here.

We update the deformation analysis of the TSB through 2020 using the TDEFNODE software (McCaffrey, 2009, 2021) to simultaneously invert InSAR interferograms, GPS time series, and leveling data for transient volcanic deformation source parameters. Our goals are to estimate how the rate of volcanic deformation varied through time and to understand sources that can reproduce the measured deformation, including both elastic and viscoelastic models.
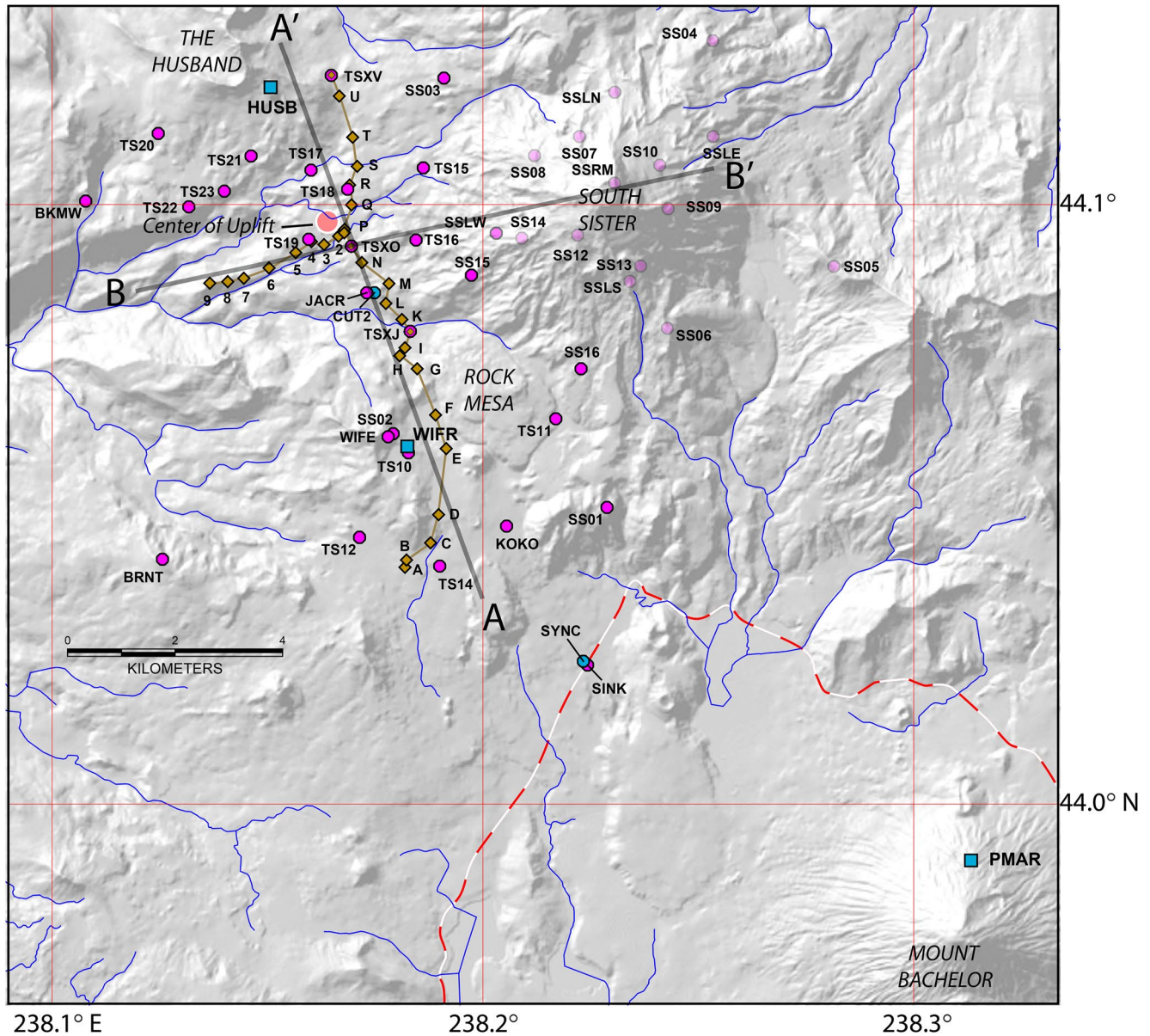
2. Data

2.1. InSAR-Measured Maps of Range Change

We selected ERS, ENVISAT, TerraSAR-X, Sentinel-1, and RADARSAT-1 synthetic aperture radar image pairs for the period 1992.4–2020.8 based on orbital separation (<500 m) and snow-free intervals, which yielded 63 unwrapped interferograms (Table S1). These interferograms were the best with respect to coherence and signal-to-noise ratio and, except for the last three years of Sentinel 1 scenes, were chosen by inspection to represent the deformation field. For the last three years of Sentinel 1 interferograms, the number of scenes was great enough and orbital control was good enough, that we used every summer-to-summer coherent interferogram in a weighted-average stack where each interferogram was weighted by the inverse of the standard deviation of the noise outside the deforming area but within 30 km of the center of deformation. Very noisy outlier interferograms were systematically discarded from the stack. Prior to inversion, we computed and applied a planar tilt correction to each interferogram to compensate for distortion from orbital errors. We also removed a homogeneous atmospheric signal using nearby volcanoes, outside the deforming area, when appropriate. In Wicks et al. (2002), the authors applied a parameter that allowed a linear change in line-of-sight (LOS) with change in elevation to their inversion. We determined such a linear change and applied it a priori. For the TerraSAR-X and Sentinel 1 interferograms, we used volcanoes 7–25 km from the center of deformation for the atmospheric correction. For all earlier interferograms, we used volcanoes 10–25 km from the center of deformation. To reduce the large number of highly correlated data points, we then resampled each interferogram using a model-based quadtree algorithm (Jónsson et al., 2002; Lohman & Simons, 2005; Simons et al., 2002). The sizes of the quadtree parsing windows were based on the predicted surface displacement gradients for a point source (Mogi, 1958; Okada, 1992) at 6.5 km depth, with a volume increase of 0.03 km^3, located at 121.8467°W, 44.0965°N. Two window schemes were determined, one for ascending scenes and one for descending scenes, each for a radar incidence angle of ~25°. The average number of samples used in the inversion for the interferograms is 320. The source region is oversampled with these parameters, but this is advantageous when data from different incidence angles and slightly different headings are used. The variance, calculated from the LOS data within each quadtree window, was used to weight the LOS quadtree data in the modeling and to represent the uncertainties in the LOS data.

2.2. GPS Station Time Series

The TSB lies within the Three Sisters Wilderness, where land management policies severely restrict installation of permanent monitoring stations. In May 2001, the U.S. Geological Survey (USGS), with the cooperation of the U.S. Forest Service (USFS), installed a single continuous GPS (cGPS) station (HUSB) and a short-period seis-

Figure 2. Three Sisters survey-mode GPS (sGPS, magenta circles), semipermanent GPS (SPGPS, cyan circles), continuous GPS (cGPS, cyan squares), and leveling (brown diamonds) stations. The sGPS stations on and near the edifice of South Sister shown with light magenta circles are from an Electronic Distance Meter (EDM) monitoring network that was measured with survey-mode GPS in summer 2001. The center of the uplifted area is shown with a labeled red circle. Leveling results were projected onto Lines A-A' and B-B' to produce the vertical-displacement profiles shown in Figure 6. Red-white dashed line in lower right portion of the figure is Oregon Highway 342 (Cascades Lakes National Scenic Byway).

mometer near a craggy peak known as The Husband (Figure 2). The station is located 2.5 km NNW of the center of the TSB and provides a daily measure of ground position. Intermittent gaps in the GPS data occur during the winter when either the power fails, or the antenna is partially plated by ice or buried by snow. The station was rebuilt, and the antenna was replaced in 2018 after a wildfire damaged the equipment. Other equipment changes at the station since its installation are described in Table S2.

Also in summer 2001, 16 stations from an existing USGS Electronic Distance Meter (EDM) monitoring network, last measured in 1986 (Iwatsubo et al., 1988), were recovered during a survey-mode GPS (sGPS) campaign, and several new sGPS stations were added (Figure 2). In early 2002, a second regional cGPS monitoring station, PMAR, was installed outside the wilderness near the edge of the deforming area at Pine Marten Lodge on Mount

Bachelor. New sGPS stations were added during annual surveys through 2006, bringing the total number of sGPS stations within 20 km of the center of the TSB to more than 40. In 2009, a network of 12 semipermanent GPS (SPGPS) stations was established on and around the TSB; two more stations were added in 2013 (Table S3). SPGPS is an alternative to cGPS and sGPS in which GPS receivers are temporarily deployed at permanently installed monuments that serve as force-centered mounts for the GPS antenna, eliminating the need for a tripod and tribrach and facilitating longer deployments than are practical with sGPS (Blewitt et al., 2009; Dzurisin et al., 2017). The Sisters SPGPS network was observed from early July to late August each year from 2009 to 2020.
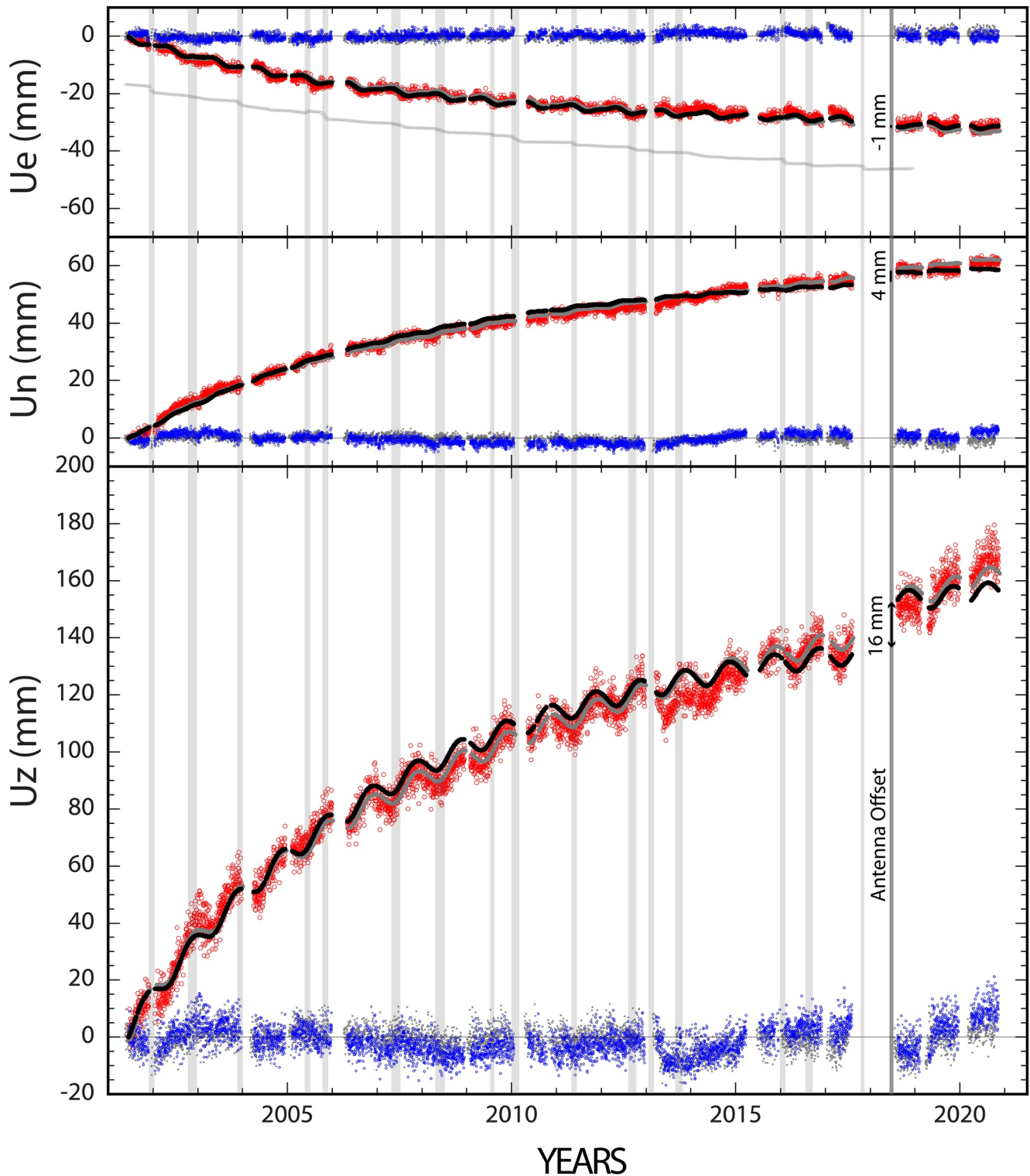
Following a small earthquake swarm in March 2004 (Dzurisin et al., 2006, 2009), the USFS approved a second wilderness volcano monitoring station (cGPS site WIFC/WIFR, and seismometer site WIFE) located south of the center of the bulge and near another craggy peak called The Wife. The cGPS WIFC/WIFR antenna mount was repeatedly damaged by snow loading and the antenna was moved to a different mount in 2008, only to suffer the same fate in later years. In 2018, the site was converted to an SPGPS station to be deployed only during summer months.

We analyze time series of daily GPS station positions produced by the USGS Earthquake Hazards Program (Murray & Svarc, 2017). We use the raw, trended time series from their filtered NA-fixed reference frame and weight the data using their a priori uncertainty. The filtering reduces common-mode noise in the time series by applying small daily network transformations estimated from a subset of regional stations with steady long-term velocities (Murray & Svarc, 2017). Station offsets and outliers are estimated separately using the methods of Langbein (2004, 2008, 2012), which include a temporally correlated noise model, followed by visual inspection; they are supplied as input to the TDEFNODE analysis. This noise analysis and a comparison with the a priori uncertainties are discussed in the Supporting Information S1 (GPS data precision, Tables S4 and S5). We conclude that for our study the a priori errors are about twice those estimated with the noise analysis.

Throughout the paper, we use the GPS (Global Positioning System) acronym rather than the more general GNSS (Global Navigation Satellite System) because our daily position solutions are derived only from NAVSTAR GPS satellite data.

The HUSB time series (Figure 3) demonstrates that the deformation has increased smoothly since 2001. The data were corrected for estimated steady background tectonic motion (1.1 mm/yr East, 4.5 mm/yr North, −1 mm/yr Up) to isolate the volcanic signal. Seasonal perturbations and an antenna offset (See Table S2 for a list of all equipment changes at station HUSB) were identified in the time series and estimated along with exponential and log rates of decay. The estimated exponential rate of decay τ in the equation $A\left(1 - e^{-t/\tau}\right)$ is ~6.5 years. The estimated logarithmic rate of decay τ in the equation $A\left(log10\left(\tau + t\right)\right)$ is ~1 year. As seen in Figure 3, the residuals from the decay model with seasonal and offset corrections applied are generally small, but there is some variation with time. The exponential decay tends to underestimate the rate of decay at the start and end of the time series, while overestimating the rate of decay in the middle of the time series. The log fit is better in the middle and end of the time series. Residuals from both fits show small, but systematic trends in the 2012–2016 interval. The background tectonic motion is estimated using a block rotation model for the horizontal components, while the vertical rate of −1 mm/yr is an average of all cGPS stations used outside of the TSB (most of the red dots in Figure 1). Note that small changes in these values will change the estimated decay constant, τ, for both the exponential and log fits. In our TDEFNODE analysis of all GPS data, we simultaneously solved for volcanic source models and background tectonic motion to minimize the tradeoff between tectonic and volcanic source parameters. Note that, unlike the GPS station time series shown in Figure 3, those shown in the Supporting Information S1 are corrected for seasonal perturbations and antenna offsets.

GPS sites near Three Sisters are only slightly deflected by the numerous slow-slip events (SSE) at the Cascadia Subduction Zone (Figure 3 and Figure S1a), and we did not model them explicitly. These events occur about every other year and offset the time series less than 3 mm (Figure 3). For the ~20-year-long time series we used where the SSE are short duration (weeks) relative to the long-term volcanic deformation, we considered SSEs to contribute to the steady-state background site velocities that arise from block motions and elastic strain rates due to Cascadia locking (McCaffrey et al., 2013). See Schmalzle et al. (2014) for a more complete description of slow slip behavior in this section of the Cascadia Subduction Zone.

Figure 3. Time series plots of East, North, and Up (top, middle, bottom, respectively) daily average displacement of cGPS station HUSB, located in the Three Sisters Wilderness about 2.5 km north-northwest of the center of inflation. The displacements (red) are corrected for estimated tectonic background movements of 1.1 mm/yr East, 4.5 mm/yr North, and −1 mm/yr Up. The modeled displacement (black) includes an exponential fit, annual and semi-annual seasonal perturbations (sinusoidal undulations), and an antenna offset (time marked by dark vertical line in 2018). The residuals (blue) are the difference between the model and the observations. Modeled results and residuals from a log fit to the data are shown in gray. Light gray vertical lines mark times of slow slip events, and the sloping light gray line in the east plot shows estimated offsets from these events superimposed on volcanic motion (hence, the nonzero slope).

Due to its proximity to the TSB and daily position estimates, the HUSB time series has the best temporal resolution and highest precision of all available geodetic datasets. The smoothness of the HUSB time series is not easily reconciled with the piecewise linear time history with a kink during 2004, as proposed by Riddick and Schmidt (2011). Note especially that the better resolved North and East (relative to Up) components of motion at HUSB show no kink in 2004, including at the time of the March 2004 earthquake swarm. The HUSB time series was cited by Rodríguez-Molina et al. (2021) as the strongest evidence that the decay in inflation rate was exponential and hence due to viscoelastic relaxation of the crust. By including other data, we find that exponential decay does not satisfy HUSB and other observations simultaneously until after 2005 (see Discussion, Viscoelastic relaxation).

2.3. Leveling Data

Elevation differences between survey marks with an average spacing of 560 m were measured by leveling along the James Creek and Separation Creek Trails, which intersect within 1 km of the center of uplift (Figure 2). The north-south traverse along James Creek Trail (marks A–V) is 13.6 km long and the east-west traverse along Separation Creek Trail (marks 1–9) is 3.2 km long (stadia distances). Marks I through V and 1 through 9 were surveyed in 2002, 2003, 2004, 2005, 2006, and 2008. Marks A through V and 1 through 9 were surveyed in 2005, 2006, and 2008. The surveys followed standards and procedures for first-order, class II surveys. Small corrections for rod scale, rod temperature, level collimation, and refraction were applied to observed elevation differences to obtain the data used here. See Dzurisin (2021) for additional details.

3. Modeling Strategy and Inversion Method

We combined InSAR interferograms, repeated leveling profiles, and three-component GPS station time series to understand better the transient volcanic deformation associated with the TSB. We used the updated program TDEFNODE (McCaffrey, 2009, 2021) to estimate parameters representing the time-dependent variations in buried volcanic source(s). The GPS data span 1999.1–2020.7, the 63 InSAR interferograms span 1992.4 to 2020.8, and leveling data span 2002.6 to 2008.6 (Figures S2–S7, Tables S1 and S6; Dzurisin, 2021). Our modeling attempted to fit all these observations simultaneously by a weighted, least squares inversion. As noted earlier, continuous GPS recordings were not available until mid-2001, so our estimate of the inflation history from 1995 to 2001 relies solely on InSAR data (Wicks et al., 2002).

For elastic half-space volcanic source representations, we used a standard Mogi point source (Mogi, 1958), a planar, horizontal, uniform-displacement tensile source (sill) (Okada, 1992), and a finite, vertical prolate spheroidal source (Yang et al., 1988). For time dependence in the rate of source volume change for the elastic models, we chose between a general time increment sampling method where expansion rate or opening rate between samples is linear or discrete time segments of constant rate (producing a piecewise linear surface displacement function). Details of the methods are provided in the Supporting Information S1.

In addition to the elastic models, we included one where the temporal decay in surface deformation is produced by viscoelastic relaxation of an aureole of crust surrounding the magma body. In this case, the injection of magma is an instantaneous event into a spherical cavity as described by Segall (2010; p. 240), and the deformation rate observed at the surface decays in exponential fashion due to crustal relaxation (see Supporting Information S1 for details of viscoelastic model implementation). We allowed for continued injection in all models, including those with a viscoelastic shell.

At any point (x, y) and time t on the Earth's surface we calculate a three-component (East, North, Up) displacement time series $\mathbf{D}(x,y,t,P_k)$ from the set of parameters P_k that describe tectonic motions and transient sources. To match the observed three-component GPS time series $\mathbf{G}(x,y,t)$ for a given site, we estimate the static offset X_o between the observed and calculated signals, a linear term representing steady velocity V, and for cGPS only, seasonal terms with amplitudes of A_1 and A_2:

$$\mathbf{R}(x,y,t) = \mathbf{D}(x,y,t,P_k) - \mathbf{G}(x,y,t) - X_o - V(t - t_o) - A_1 \sin(2\pi t) - A_2 \cos(2\pi t) \tag{1}$$

where $\mathbf{R}$ is the residual and time t is in years.

The GPS displacement time series we use are in a fixed North America reference frame and our modeling can account for secular tectonic motions in that reference frame. Regionally, the steady geodetic surface velocities arise from a combination of crustal block rotations, elastic strain rates from friction on faults, and distributed permanent crustal strain rates. The site velocities V are estimated either by solving for each GPS slope independently or by using a simple block model. The latter approach requires many fewer free parameters (12 instead of one each for the ~300 GPS time series) and imposes spatial correlation among the velocities, but it has the disadvantage of being more sensitive to velocity errors. For example, a misfit of only 0.1 mm/yr in rate leads to a position error of 2 mm after 20 years.

The time-dependent rate of volume increase in a cavity embedded in an elastic half-space is given by:

$$s(t) = A(P_k)S(t) \tag{2}$$

where A is the amplitude due to a set of source parameters P_k. The time dependence $S(t)$ of the source volume change rate can be set to one or more boxcar functions (a constant rate of volume increase in a given time interval), or a series of overlapping triangles (a linear rate of volume increase with time in a given interval) as is done for earthquake time functions (e.g., McCaffrey, 2009; Nabelek, 1984; Figure 1, Supporting Information S1). For a given volumetric source, the free parameters for the discretized time history $S(t)$ are T_o, the origin time, and the triangle or boxcar amplitudes B_i, ($i = 1, N$ where N is the number of elements in the time function). The rise-time of the triangle or duration of the boxcar (τ; McCaffrey, 2009) is fixed at 270 days; other durations were tested and had no impact on the result (Figure S1b). The surface displacement history in all cases was found by integrating $S(t)$ over time and applying the Green's functions for the appropriate spatial source.

To match the observed InSAR LOS displacements $I(x, y)$ for a given interferogram, the surface displacement $\mathbf{D}(x, y, t, P_k)$ is projected along the look vector $\mathbf{L}$:

$$R(x, y) = I(x, y) - \left[\mathbf{D}(x, y, t_2, P_k) - \mathbf{D}(x, y, t_1, P_k)\right] \cdot \mathbf{L} - B_o \tag{3}$$

where t_1 and t_2 are the times of the two scenes comprising the interferogram and B_o is a static offset term.

Leveling data, in which differential vertical displacements are estimated between surveys, are treated in a similar fashion to InSAR, where the look vector is set to (0,0,1).

To find the best estimates of the parameters P_k, the methods of simulated annealing (Press et al., 1989) and grid search were applied to minimize the sum of the weighted residuals squared, plus penalties. Penalties were applied to keep some parameters within bounds, such as to keep the Mogi source below ground level, for example. Each observation was weighted by the inverse of its variance, but we did not use the data covariance in the calculations. In addition to the parameters describing the spatial and temporal features of the subsurface source, there are others related to the optimization of the data, namely estimates of slopes and offsets for each of the three components of 104 GPS time series, estimates of seasonal signals in the 18 cGPS (two terms for each of three components), LOS offsets for the 63 interferograms (one for each), and vertical offsets for the 10 leveling profiles (one each), totaling ~800 parameters (Table 1). These parameters are estimated by a linear least squares inversion at each step of the simulated annealing or grid search. When we use a block model to estimate the GPS velocities, the 312 slope parameters reduce to the 12 that describe the rotation and strain rates of two blocks, for a total of 493 free parameters.

4. Modeling Time Dependence in Source Volume Change

We ran numerous models to test features of the possible sources and constraints provided by the data, a subset of which is described in Table 1. We describe the model setups and general results in this section and discuss results in detail in the next. The model region was limited to the area from 236.9°E to 239.5°E and 43.1°N–45.1°N, with the TSB in the center. The interferograms spanned from ~238.0°E–238.3°E and from 43.9°N to 44.3°N and covered most of the deformation.

The simplest model is a Mogi or spherical point source at depth in an elastic halfspace and a time history comprising a series of overlapping triangles (model sis1) or boxcars (model sisL). The time history in our models starts at 1992.5 and continues until 2020.5 (Figure 4a). The free parameters are the latitude, longitude, and depth of the source and 38 amplitudes of the injection rate (in millions of cubic meters per year, Mm³/

Table 1
Model Parameters and Fits

Model	Type	Red Chi²	Nrms	cGPS Nrms	SPGPS Nrms	sGPS Nrms	InSAR Nrms	Level Nrms	P1	P2	DOF	Ndata	Depth	Lon	Lat	Volume
sis1	Mogi, Triangles	1.11	1.05	0.92	0.96	0.98	1.38	1.41	40	807	129,269	130,116	5.90	0.00	0.00	49.4
sisL	Mogi, Boxcar	1.11	1.05	0.92	0.96	0.98	1.36	1.27	41	802	129,273	130,116	6.11	0.02	−0.03	52.9
sis8	Sill, Triangles	1.35	1.16	0.99	0.97	0.99	1.35	0.11	43	802	129,271	130,116	5.51	0.18	−0.55	35.4
sisU	Prolate, Triangles	1.10	1.05	0.91	0.96	0.98	1.37	1.76	42	802	129,272	130,116	6.78	−0.14	0.29	39.9
sisD	Mogi R&S	1.10	1.05	0.92	0.96	1.00	1.52	2.25	8	807	129,301	130,116	6.05	0.02	−0.02	52.0
sisN	Sill R&S	1.24	1.11	0.98	0.96	1.00	1.51	0.65	9	807	129,300	130,116	5.70	0.08	−0.54	37.2
sisZ	Mogi, blocks	1.84	1.35	1.32	1.23	1.65	1.31	1.66	59	493	129,632	130,184	5.77	0.02	0.11	47.8
sisE	Mogi Exp, post-2000	0.86	0.92	0.91	0.96	0.90	0.00	1.78	39	739	107,627	108,405	5.64	0.07	0.06	11.5
sisF	Mogi Exp	1.10	1.03	0.92	0.96	0.98	1.18	1.12	55	802	129,259	130,116	6.28	0.02	−0.02	20.6
sisO	Mogi exp, pre-2000	1.15	1.07	0.93	0.96	0.98	1.21	0.56	19	802	129,295	130,116	6.05	0.08	−0.11	5.4
Ndata				81,216	25,416	2907	20,211	252								

Note. Red Chi2, reduced chi-square, sum of R^2/S^2 divided by DOF; Nrms, normalized RMS, square root of (sum of R^2/S^2 divided by Ndata); Ndata, number of observations of a given type (cGPS, SPGPS, InSAR, etc.); P1 - number of parameters related to transient source; P2, number of parameters related to offsets, slopes, seasonal signals; DOF, Ndata minus total parameters (P1 + P2); Depth - depth of center of source in km below ground surface; Lon - difference in km from source of sis1 (238.164°E); Lat - difference in km from source of sis1 (44.098°N); Volume, volume added, in Mm³; Exp, exponential; See Section 3, Modeling strategy and inversion method, for explanation of other terms (Triangles, Boxcar, Blocks, etc.); R&S, Riddick and Schmidt (2011).

yr = 10^6 m³/yr). In these model runs, the slopes of the individual GPS time series were estimated independently of one another.

The best-fitting location for the Mogi source is at 238.164°E and 44.099°N, about 5 km west of the summit of South Sister volcano (Figure 2), at a depth of 4.1 km below sea-level (see Figures S2–S7 for details of the model fit to specific GPS, InSAR, and leveling data). Because we correct for the elevations of the observation points by offsetting the source depth (Williams & Wadge, 1998), the depth of the Mogi source below the ground surface is closer to 5.9 km, considering the average elevation in the source area is about 1.8 km. Formal one-sigma uncertainties estimated by linearizing the inversion at the best-fit model are 0.0001° (about 100 m) in latitude and longitude and 0.03 km in depth. These surely underestimate the actual uncertainties because many of the data are not fully independent of one another. For the various models we ran, the best-fit depths vary from 5.3 to 6.7 km below ground and within a half-kilometer of the Mogi location (Table 1). Fits to selected interferograms and results of the quadtree interpolation are shown in Figure 5 and all interferograms are shown in Figures S5 and S6. Fits to all GPS time series are shown in Figures S2–S4, and leveling fits are in Figure 6 and S7.

Smoothing, or damping, is applied to the estimated inflation rate time series by adding a penalty proportional to its second derivative calculated at each sample time (McCaffrey, 2021). We first tested the impact of damping on estimates of the inflation time history (Figure 4a). With an increased damping coefficient (where 0 is undamped) the fit becomes worse, but the history of inflation becomes smoother and the peak inflation rate is depressed. We decided on a moderate damping (coefficient of 0.05) that damps the high oscillations but does not completely flatten the curve (red curve in Figure 4a). Notable are quasiperiodic peaks in inflation rate (injection pulses) every 3–4 years. The largest peak occurred during 1997–1999. Thereafter, the inflation rate generally declined, but smaller pulses are evident throughout the ensuing two decades. The pulses are robust features of all models, whether elastic or viscoelastic, that adequately fit the geodetic data (see Discussion).

In model sisZ, the Mogi model and inflation history were the same as discussed above, but we allowed the GPS site velocities to be determined by a simple block configuration in which two blocks comprised the domain region and were separated along the arc (~238.2°E; Figure 1). Each block was allowed to rotate and to strain at a uniform rate. The strain rate simulated the contraction due to the Cascadia subduction zone. Because the relative slip rate is very low, we did not include elastic strain arising from the fault bounding the two blocks.
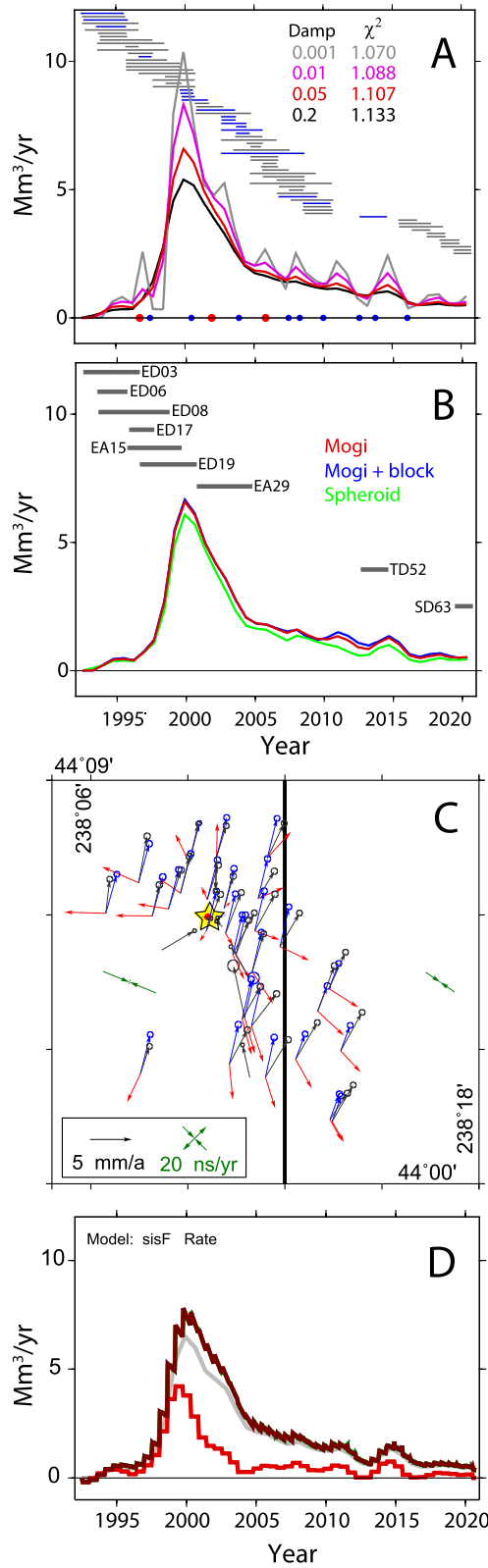
Figure 4.

The parameters describing the angular velocity (three for each block) and strain rate (three for each block) were estimated simultaneously along with the transient source parameters. The blocks were large enough (over 100 km on a side) to include many GPS stations not impacted by the volcanic deformation. Hence their velocity parameters are effectively independent of the transient deformation. This allows a more robust estimate of the background linear velocities of the sites within the zone of deformation.

Another model we tested was that of a horizontal, planar, rectangular crack opening vertically, the sill model (sis8). The free parameters for this run were longitude and latitude of the crack, the East-West and North-South dimensions of the crack, its depth, and the time-dependent vertical opening rate in mm/yr sampled every 270 days, as was done for the Mogi source. The estimated depth was 5.5 ± 0.08 km below ground level, similar to the Mogi model, and the best-fit crack dimensions were equidimensional, 6.6 by 6.6 km. The maximum opening rate was in late 1999 at 62 ± 5 mm/yr (Figure S1c).

In addition, we examined the possibility of the source being a prolate spheroid (model sisU; Davis, 1986; Yang et al., 1988). In this case we used the same temporal approach as in model sis1. The spheroid was constrained to be vertical with a semi-minor axis of 1 km. We solved for the latitude, longitude, and depth of the center of the spheroid as well as the ratio of the semi-major to semiminor axis. The location of the spheroid was similar to the Mogi source but slightly deeper, 6.8 ± 0.04 km below ground level. The estimated ratio of the axes was 1.2, very nearly a sphere, like the Mogi source. The spheroid source fit the data slightly better than the Mogi sphere (1.10 v. 1.11; Table 1) but we think this small difference is not significant.
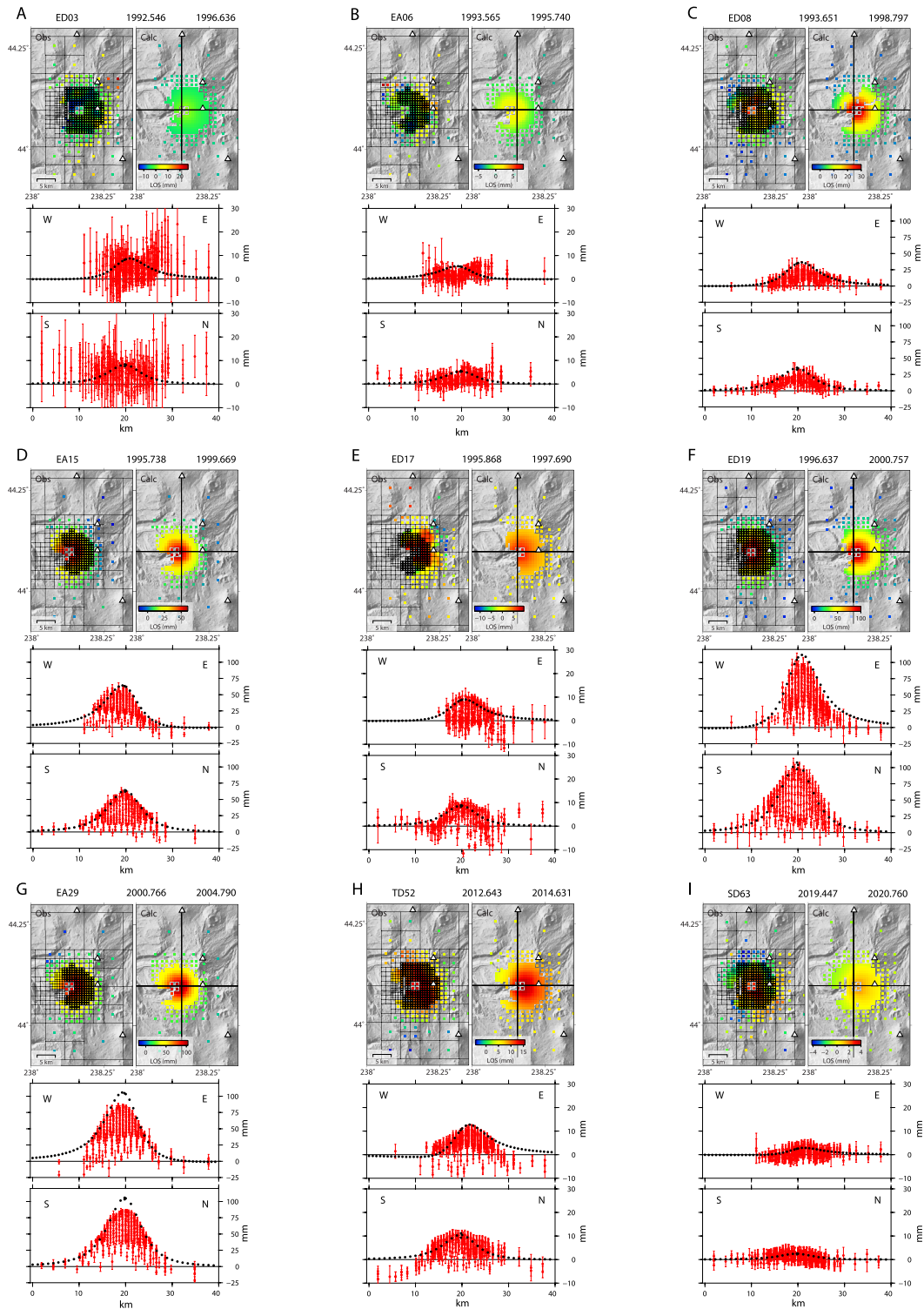
To address the suggestion of Riddick and Schmidt (2011) that the deformation history was piecewise linear (or equivalently that the inflation rate was constant over a period of time and then changed abruptly to a new constant rate), we ran model sisD. Riddick and Schmidt (2011) examined only the period 1998.5–2011 and proposed a change in inflation rate at 2004.2. Because, we modeled a longer time period, we broke it into 4 segments and during each segment the inflation rate of the Mogi source was assumed to be constant. The segments we chose included those used by Riddick and Schmidt (2011) but expanded to include short segments before and after (the segments are 1992.5–1998.5, 1998.5–2004.2, 2004.2–2011.0, and 2011.0–2020.5). This model provides an overall fit that is similar to the smoothly varying histories, but the visible misfit to the HUSB time series argues against it (see Discussion, Piecewise linear inflation).

Finally, we developed a model in which a spherical magma body sits within a larger shell of Maxwell behavior, based on Segall (2010). In this case, the decay in the deformation rate is largely due to relaxation of the viscoelastic shell following injection into the central sphere. As discussed in detail later, we found that this type of model fits the observations quite well with considerably less magma input than the elastic models. We recognize that, as is always the case for solutions of an inverse problem, our best-fit models are nonunique. They are plausible representations of the deformation source geometry and mechanism, based on stated assumptions and constrained by available observations.
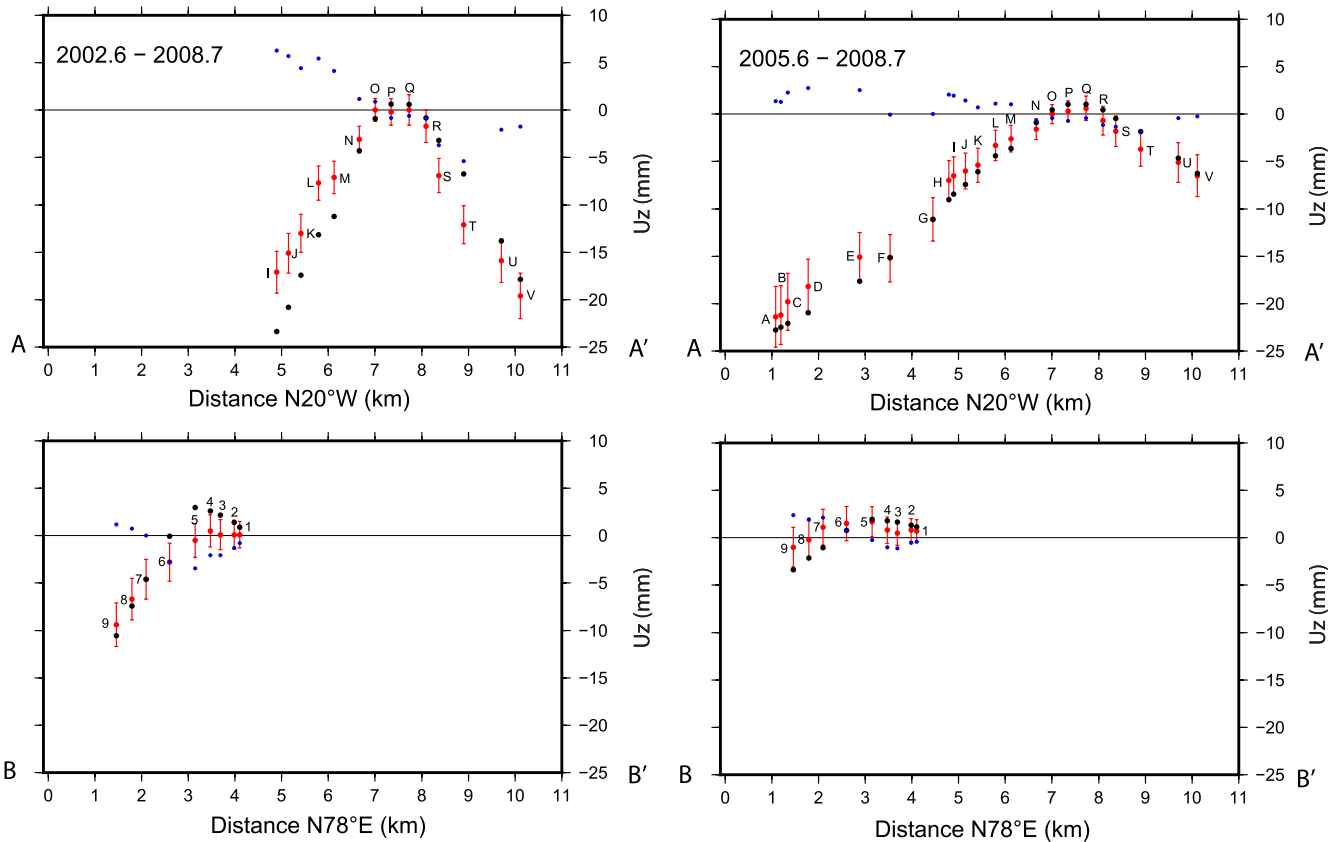
5. Discussion

We tried multiple geometrical and rheological source models: Mogi, sill, and prolate spheroid in an elastic half-space, and Mogi within a viscoelastic shell. Each of the geometries predicts a particular pattern of surface deformation. For a Mogi source, the 3-D ground displacement at the surface is radial to the source and its amplitude de-

Figure 4. (a) Effect of smoothing on estimates of the inflation rate history for a Mogi source. Horizontal bars show the spans of the interferograms, and the color indicates level of fit (blue = $1 <$ Nrms ≤ 3; gray = Nrms ≤ 1). Dots along the timeline mark occurrences of SSE near the TSB, from Schmalzle et al. (2014) and updated by R. McCaffrey. Red dots are those with more than 2 mm west predicted displacement at HUSB and blue are more than 1 mm. (b) Inflation rate histories for Mogi model where background velocities are independent (sis1, red), Mogi model where background velocities are from block model (sisZ, blue), and the vertical prolate spheroid model (sisU, green). Note apparent quasiperiodic pulses in inflation rate both before and after the main pulse in 1998–2001 (a, b; see Discussion). (c) Comparison of estimated horizontal site velocities for Mogi model where background velocities are independent (sis1, gray) and Mogi model where background velocities are from a block model (sisZ, blue). Yellow star shows the peak of TSB uplift and red arrows show the average velocities of the GPS sites from 1992.5 until 2000. Green arrows are the strain rates in the two regions estimated in model sisZ. (d) Inflation rate for model sisF where a spherical source at depth is surrounded by a viscoelastic spherical shell. The source volume change is represented by 200-day time periods during which influx is constant (boxcar) followed by relaxation of the outer shell. Red curve shows the influx rate in Mm^3/yr and the brown is corresponding signal in the elastic region outside the viscoelastic shell. In 2000, the influx largely ends and the shell relaxes, giving the exponential decay with small pulses superimposed. Light gray curve shows the results of purely elastic response (sis1).

Figure 5. Examples of the 63 interferograms used in this work (Table S1). The first letter of the 4-letter code at the top refers to the SAR satellite: E–ERS, T, TerraSAR-X, S, Sentinel-1; second letter is A for ascending orbital path and D for descending; and the following two-digit integers are in chronological order (see Supporting Information for additional interferograms). To the right of the code are the dates of the first and second scenes used. For each interferogram/profile pair: Top left panel shows observed line-of-sight (LOS) changes with positive indicating decreasing distance (toward the satellite) and the grid used for quadtree interpolation. Top right panel shows predicted LOS changes after interpolation, and the lines of the S-N and W-E profiles. Bottom panels show LOS observations in red projected onto W-E and S-N profiles. Black dots show the predicted LOS changes for the Mogi source (sis1). The profiles intersect at the Mogi source estimated by the inversion. Note that the LOS scale changes from panel to panel to enhance visibility.

Figure 6. Vertical displacements from leveling surveys (red dots with 1-sigma error bars), model fits (sis1, black dots), and residuals (blue dots) along north-south and east-west traverses (top and bottom, respectively) for two intervals: August 2002–2008 (left panels) and August 2005–2008 (right panels). Labels A–V and 1–9, benchmark ID. Marks I through V and 1 through 9 were surveyed each summer from 2002 to 2008. Marks A through V and 1 through 9 were surveyed in 2005, 2006, and 2008; hence the longer north-south profile in upper right panel.

creases by the inverse square of the radial distance from the source. That is, the ground deformation is maximum and vertical directly above the buried cavity, and it becomes much smaller and subhorizontal at radial distances of several source depths. Relative to a Mogi source, horizontal displacements are smaller for sill-like sources and larger for vertically elongate prolate spheroidal sources. Accordingly, multiple well-distributed geodetic datasets should have ample sensitivity to the actual source geometry.

We assessed the models based on both visual fits and statistical measures. We did not do formal statistical tests because our data do not obey the Gaussian distribution required. Many of the observations are spatially and temporally dependent and therefore it is difficult to know what the degrees of freedom are for any given model. Nevertheless, we present the reduced chi-square misfits as a guide (Table 1), with the point that there are many more data (~130,000) than free parameters (<800), so the number of degrees-of-freedom is large. Reduced chi-square can be compared from model to model, though computing probabilities is probably not helpful.

5.1. Mogi Source With Block Model

For many of the models, the steady rates of motion of the individual GPS time series were estimated by regression simultaneously with the magmatic source parameters. This approach is robust because the magmatic deformation pattern provides spatial correlation among the GPS sites. However, some parameters, such as the decay constant in exponential models, depend on having a reliable estimate of the background rate (slope of the time series). To this end, we first estimated the regional crustal deformation and took some site velocities from that motion. We broke the region into two blocks along the arc (Figure 1) and estimated rotation and strain rates for them along with the Mogi deformation while satisfying the data. For this model only, we included velocities of nearby sites estimated by McCaffrey et al. (2013) that contribute to the estimate of long-term motion. In addition to the hori-

zontal velocities, we estimated a vertical bias for each of the GPS time series groups (cGPS, sGPS, and SPGPS) and found the vertical bias to be about −1 mm/yr for all three groups.

The time dependence of the Mogi source estimated in this model (sisZ) was very similar to that of model sis1 (Figure 4b), and the predicted site velocities were similar as well (Figure 4c). The rotation of the blocks moves them more-or-less northerly relative to North America (Note that because we are estimating strain rates along with the rotations, these are not Euler poles, that are defined for a rigid spherical shell.). The principal strain rates estimated in this manner were about 39.0 ± 0.8 nanostrain/year contraction at $109° \pm 1°$ azimuth west of the arc, and 21.6 ± 0.2 nanostrain/year at $121.4° \pm 0.3°$ azimuth east of it (Figure 4c). These contraction rates and directions are consistent with accumulating strain from the Cascadia subduction zone seen all along the fore-arc (McCaffrey et al., 2013; Schmalzle et al., 2014). The orthogonal, northerly strain rates were small (<2 nanostrain/year) and contractional, indicating no shear along the arc. In the following models, we constrained the velocity estimate for HUSB.

5.2. Mogi Source

Figure 4a (red curve) shows our favored elastic halfspace estimate of the injection rate to a Mogi source as a function of time. Formal uncertainties in the inflation rate are less than about 1×10^6 m³/yr before year 2000 and less than 0.2×10^6 m³/yr after 2000, when GPS data became abundant. The modeled time begins at 1992.5, but there is little evident inflation before late 1995 or 1996. Because there were no cGPS or nearby sGPS sites operating at this time, the resolution of the onset time is based on InSAR observations that have at best a one-year sampling interval. The onset time is discussed in more detail below. The inversion shows that the peak in inflation rate occurred in late 1999 at about 7×10^6 m³/yr (although this value depends on the damping used). The modeling suggests that intrusion began sometime in late 1995–1996 and increased in rate substantially from 1997 to 1999; thereafter, the rate began to decay. The use of boxcar time function elements instead of triangles (sisL) gives nearly identical results (Table 1, Figure S1d).
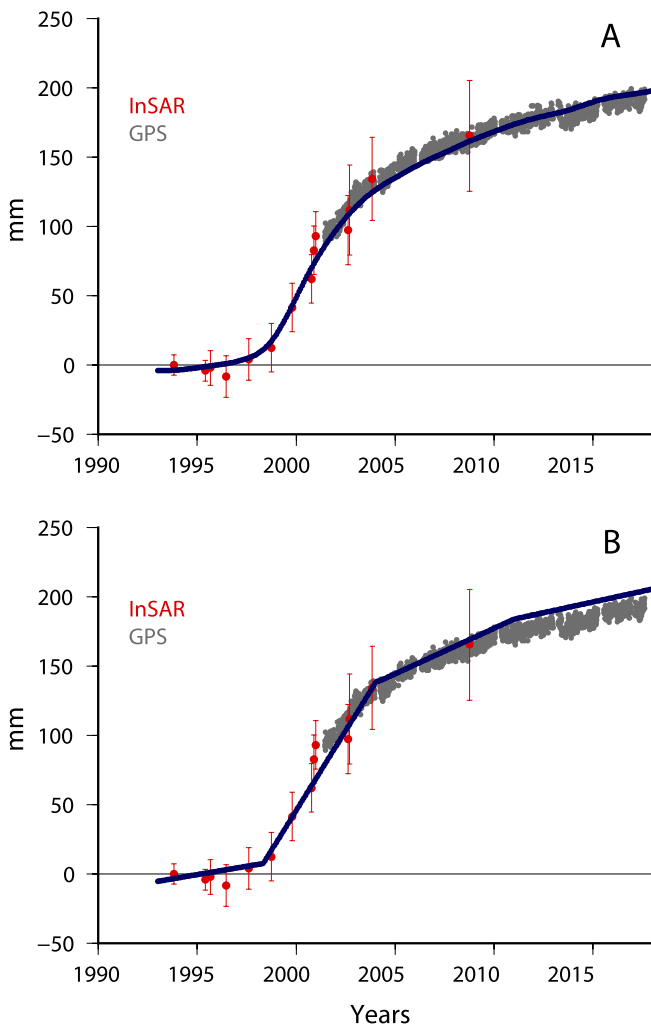
5.3. Prolate Spheroid

The inversion for the prolate spheroid resulted in the ratio of the axes approaching unity, or basically a sphere, the Mogi source. The fit to the data for the spheroid model (sisU) is less than 1% better than for the Mogi model (sis1; Table 1; Figure S1e). Hence, we rule out a prolate spheroid that significantly differs from a sphere.

5.4. Sill

The sill model (sis8) assumes a horizontal flat crack that opens vertically. The size of the sill rectangle is estimated at 6.6 by 6.6 (±0.08) km at a depth of 3.9 km below sea level (5.5 km below ground surface). The fastest rate of opening was about 62 mm/yr in late 1999 and the total opening reached 72 cm by mid-2020 (Figure S1c). By 2020.5, the estimated volume of the sill was about 35.4×10^6 m³. The sill model provides an overall poorer fit to the data relative to the Mogi source (sis1 vs. sis8; Table 1). The fit to the cGPS site HUSB time series is diagnostically poor (Figure Sf). The vertical component of motion (Up) is fit well, but the amplitudes of the North and East components are underestimated. Accordingly, we conclude the source geometry is not likely to be that of a dilating sill.

5.5. Piecewise Linear Inflation

The main argument against piecewise linear inflation as proposed by Riddick and Schmidt (2011) is the continuous GPS time series recorded at HUSB (Figures 3 and S1g). While their model predicts a kink in the deformation rate time series around 2004.2, the HUSB data show smooth curvature through that time. Riddick and Schmidt (2011) did not use the GPS data other than HUSB and their InSAR time series is sampled at about a one-year interval, so temporal resolution is lacking. In Figure 7, we convert the HUSB GPS time series to an equivalent line-of-site change and re-scale the Riddick and Schmidt (2011) InSAR time series to the position

Figure 7. Comparison of (a) smooth (sis1) and (b) piecewise linear (sisD) model fits to the displacement history at cGPS station HUSB. For the comparison, the HUSB 3-component displacement time series (Figure 3) was converted to an equivalent line-of-sight (LOS) time series (gray dots), and the Riddick and Schmidt (2011) InSAR time series was re-scaled to the position of HUSB. The InSAR time series is fit within uncertainties (red dots and error bars) by both models, but the HUSB time series is better matched by our preferred smooth model sis1. See text and Supporting Information for details of models sis1 and sisD.

of HUSB. Their InSAR time series appears to fit either the smooth (top) or piecewise linear (bottom) model, but the HUSB time series is better matched by the former.

5.6. Viscoelastic Relaxation

From abundant continuous and episodic GPS coverage, the decay in the deformation from 2000 to about 2010 as recorded at HUSB can be well described as exponential (Figure 3). This could be caused either by an exponential decay in the rate of magma injection into the Mogi source (if the crust responds elastically), or by viscoelastic relaxation of the crust following one or more short-lived injection events sometime during late 1995–1999. These two possibilities are indistinguishable from the available data.

As described by Segall (2010, Equations 7–105), a spherical cavity enclosed in a spherical shell of viscoelastic material subjected to an instantaneous injection event can produce a surface deformation whose rate decays in an exponential manner (see also Supporting Information S1). The decay constant depends on the material properties of the shell and the radii of the cavity and the shell. The instantaneous displacement at the surface mimics a Mogi source.

The HUSB cGPS time series can be fit well by an exponential function when the sGPS and SPGPS data after 2000 (HUSB started in 2001.5) are included in the model, but the InSAR data are excluded (Figures 3 and S1h; sisE). However, when the InSAR data are added, the fit to HUSB is poorer (Figure S1i; sisF). The additional data result in a small (<1 km) change in the position of the source such that the relative amplitudes of the East, North, and Up components at HUSB are misfit. They change by about 10 mm over the 20-year span of the data.

The viscoelastic shell model represents the deformation utilizing a different set of parameters than a simple decay fit. We fix the radius of the inner sphere R_1 while solving for the radius of the viscoelastic shell R_2, the depth, longitude, and latitude of the center, and the log of the viscosity of the viscoelastic shell. The relaxation time (Segall, 2010, Equations 7–98) depends on the viscosity and outer radius R_2, which are free parameters, as well as the inner radius ($R_1 = 1.0$ km), and the elastic constants Poisson's ratio (0.25) and shear modulus (4.0×10^{10} N/m^2), whose values are set. R_1 and R_2 impact the amplitude of the post-intrusion deformation as well as the relaxation time.

To model this mechanism with magmatic injection as a time-varying process, we estimated the rates of multiple, time-offset boxcar (constant rate) injection events of 200-day duration, converted them to volume changes, computed the relaxation history for each, and summed them. We found that this model can fit the HUSB time series well for the period after year 2000 if the InSAR data are excluded, as noted above (Figure S1h; sisE). Including the InSAR data and allowing deformation to start at 1992.5 (Figures 4d and S1j, sisF), the initial fit to HUSB is off by ~5 mm in 2000 but agrees well by 2005 and thereafter (Figure S1i).

The fit of this model sisF is as good as any of the others, with a reduced chi-square of 1.10 (Table 1) indicating that we cannot rule out a viscoelastic response to a short-lived, predominantly pre-2000 loading of the source volume. According to this model, the volume of the spherical source has increased by about 21×10^6 m^3 (Figures 4d, S-1j). To test whether source inflation ended by year 2000, we ran a model (sisO) in which flux into the inner sphere ended in 2000 and the post-2000 deformation was due only to viscoelastic relaxation (Fig. S-1k). This resulted in an increase in the data misfit by about 5% (Table 1) but required only about 5×10^6 m^3 volume

addition prior to 2000. The volume change depends on source depth and radii of the inner and outer spheres, which are poorly known. If the outer radius R_2 of the viscoelastic shell increases, as in this case where it increased to 2.0 km compared to 1.4 km for sisF (where R_1 was 1.0 km in both cases), the required input volume can be greatly reduced. As R_2 gets closer to R_1, the volume increase needed approaches the Mogi elastic case. The difference in the fits is in fitting the post-2000 undulations that are apparent in other models. In other words, a purely viscoelastic post-2000 model fits the observations only slightly less well than one that includes post-2000 small pulses in the inflation rate superimposed on a general exponential decline.

The estimated parameters change between the two tests, we think because in the latter test sisO, where injection stops before 2000, the exponential decay constrains them for a period of 20 years. With and without post-2000 inflation, respectively, source depth is 6.3 and 6.0 km, R_2 is 1.4 and 2.1 km, while estimated viscosity of the shell is 5.9×10^{17} and 6.1×10^{17} Pa-s, the latter corresponding to a relaxation time of 8.1 years. The viscosity values are consistent with those for hot crystalline rock in volcanic environments. For example, Newman et al. (2006) used a viscosity of 10^{16} Pa-s to model a viscoelastic shell surrounding the magma reservoir at Long Valley Caldera, and they cited experimental evidence (Luan & Patterson, 1992) that quartz-bearing country rocks around 350°C have viscosities between 10^{17} and 10^{19} Pa-s.

We envision two end-member scenarios. If the Earth surrounding the source is elastic, then surface deformation is a direct measure of an intrusion that continues to the present time, though greatly diminished in rate from its peak in late 1999. Alternatively, if the Earth behaves in a viscoelastic manner close to the intrusion site, it is possible that the main intrusive event occurred prior to year 2000, and since then surface deformation reflects mostly continuing relaxation of the crust. The two possibilities make very different predictions about the total volume of magma intruded. For the elastic case, it is nearly 50×10^6 m^3, while the viscoelastic case requires about 21×10^6 m^3. In either case, the observations are best-fit with a model that also includes a series of small intrusion-rate increases (pulses) since year 2000.

5.7. Onset of Uplift

Wicks et al. (2002) suggested that uplift commenced in late 1998 based on InSAR data. The models we ran for which the influx rate amplitudes were estimated through time generally agree with this estimate. Both the elastic (sis1) and viscoelastic (sisF) models show the first large pulse starting in 1998. In the viscoelastic case, the large influx had mostly stopped by the end of 1999, followed by smaller, longer duration fluctuations in the injection rate (see next section).

The six interferograms that end in mid to late 1995 show very little deformation above the noise level (Figure 5, S5, and S6). Of the three that end in mid-1996 (ED03, ED05, and ED12), only ED05 shows the type of deformation that is consistent with the shape of the TSB. By mid-1997 (ED11, ED17, and ED18), LOS changes in excess of 10 mm and largely in the pattern of TSB uplift are evident. Three images ending in mid-1998 (ED07, ED08, ED13) all show LOS changes in excess of 20 mm. By mid-1999 (ED14, ED15, ED22, and ED23), the LOS changes reached a level of about 50 mm. Accordingly, the deformation appears to have started slowly in late 1995–1996, and then increased substantially in rate during 1998–1999 (Figure 4a). An earlier onset is possible and could have gone undetected, given that observations in the area were sparse before 1992 and the episode has been largely aseismic but available evidence points to a slow onset in the mid-1990s and peak deformation rates during 1998–1999.

5.8. Inflation Transients

In the estimates of inflation rate histories (Figure 4a), we see oscillations with amplitudes of a few tenths of Mm^3/yr and periods of 3–4 years. We want to know if these are real, short-lived fluctuations in inflation rate or modeling artifacts caused by noise in the data.

We conducted tests using different coefficients for damping in which the oscillations persisted in their timing, though they decreased in amplitude (Figure 4a). Each model was started with a uniform expansion rate as a function of time. Nevertheless, the oscillations appeared in each test at about the same times. These tests showed that

increasing the damping resulted in increased misfit, indicating the oscillations are related to signals in the data rather than some numerical cause.

To try to uncover what data might be controlling the oscillations, we first removed any GPS data that might be driving them. The closest continuous GPS sites HUSB and PMAR and the SPGPS sites CUT2 and POTH were removed, and the inversion run (si1a). This resulted in the blue curve in Figure S11. Relative to the result that includes all the data (brown curve in Figure S11), the rapid drop in inflation rate around 2010 is diminished. We then removed the lone interferogram TD52 that spans the 2012.6–2014.6 period (other than TD52 the gap in InSAR data spans 2010.7–2015.4; Table S1). This model run (green curve; Figure S11) greatly flattened the oscillations relative to both other tests. Together, these tests suggest that the GPS data are driving the rapid decrease in inflation rate seen around 2010, and that the interferogram TD52 could drive the increase starting in 2012. We conclude the oscillations are real features of the data, not noise-related or modeling artifacts.

Another possibility is that slow-slip events (SSE) may be deflecting the GPS time series and that they are fit in the inversion by expansion transients. Times of known SSE that produced a displacement in excess of 1 mm are shown in Figure 4a. The SSE were derived from a catalog compiled by McCaffrey and colleagues by fitting cGPS data (McCaffrey, 2009; Schmalzle et al., 2014). Expected SSE displacements at HUSB are shown together with an exponential fit to the HUSB time series in Figure S1a (gray curves). The SSE are abundant relative to the inflation transients and one-to-one correlation is not evident. Moreover, the spatial deformation patterns from SSE and a Mogi source are very different, so it is unlikely that the displacements from SSE (shear on a planar fault west of the TSB) would map into a Mogi expansion event. At the location of HUSB, the ratio of East:North:Up displacements for a typical SSE is $-1:-0.4:-0.2$, while for a Mogi pulse at the TSB it is $-1:2:5$. Moreover, the SSE last two weeks at most, while the pulses in rate last three or more years. Tests using various sampling intervals show that the periodicity of the expansion events remains unchanged (Figure S1b). Finally, we looked at the possibility that precipitation variations and their impact on surface loading could give rise to the apparent oscillations. The precipitation data are fairly uniform throughout the study period except for 2012–2014 and in this period the variations are predicted to give rise to apparent volume changes that are out of phase with those observed (Supporting Information S1).

5.9. Source of Intruding Magma

The proximity of the TSB to South Sister (centered about 5 km west of the volcano's summit and extending across most of the edifice) raises the question of whether the source is associated with a crustal magmatic system beneath South Sister or with a deeper system beneath the region as a whole. Available information provides no definitive answer. In a study of global magmatic systems, Ebmeier et al. (2018) noted that InSAR observations reveal deformation ≥5 km away from the nearest magmatic vent in 24% of all cases, which they attributed to laterally extensive crustal magmatic systems. With reference to the most recent eruptive episodes at South Sister about 2.2 ka and 2.0 ka, which produced rhyolite from vents at the southwest toe and on the southeast and north flanks of the edifice, Hildreth et al. (2012, p.11) wrote: "That some 60 percent of the magma released during the younger episode issued from this uppermost vent (the Newberry flow) supports the likelihood that the rhyolitic magma reservoir lies under the South Sister edifice itself…" On the other hand, Hildreth et al. (2012) pointed out that those eruptions followed at least 15,000 years of inactivity at South Sister, while large volumes of mafic magma erupted from peripheral centers, including the extensive McKenzie Pass volcanic field to the northwest, mostly 4–1.5 ka (Sherrod et al., 2004). If, as we suggest, the TSB is a result of magma injection into the upper crust, the source of that magma plausibly could be a silicic crustal reservoir beneath South Sister or a deeper, more extensive source that has fed numerous mafic eruptions in the region during Holocene time.

6. Summary and Conclusions

Surface deformation near the Three Sisters volcanic center that began in the mid-1990s was continuing at a generally declining rate when this was written in early 2021. By simultaneously modeling all available geodetic datasets, we infer that the inflation source is approximately spherical in shape and located about 5 km west of the summit of South Sister volcano, at a depth of 4.1 km below sealevel (5.9 km below the surface). For elastic behavior of the crust, the inflation rate peaked in late 1999 at about 7×10^6 m³/yr, and net source inflation has been about 49×10^6 m³ (for a depth range of ±1 km the range is 34–67 × 10⁶ m³; Table 2).

Table 2
Range of Misfit and Volume for Model Source Depths

Depth (km)	Chi^2	Volume (10^6 m^3)
4.4	1.135	27.6
4.9	1.114	34.2
5.4	1.108	41.5
5.9	1.107	49.4
6.4	1.118	58.1
6.9	1.136	67.4
7.4	1.159	77.2

The deformation history can be explained equally well by two alternative models. In both, inflation started slowly sometime during late 1995–1996, the rate increased dramatically during 1998–1999, and then declined to the present time. Also in both cases, the geodetic data are best fit by a scenario that includes additional, small oscillations in injection rate every few years. In the first case, the crust surrounding the intrusion is elastic and the average injection rate has declined nearly exponentially since year 2000, resulting in a net volume increase of about 49×10^6 m^3. In the second case, the intrusion is surrounded by a viscoelastic shell and the deformation history is explained by a smaller injection of about 21×10^6 m^3 prior to 2000, followed by additional small injections (pulses) and relaxation of the shell.

The simplest explanation for the transients observed in Figure 4a is that they are caused by pulses of magma that occur every few years throughout the 25 years of measured deformation at Three Sisters volcanic center. The pulse temporally centered near the year 2000 is the largest of these quasiperiodic pulses. Petrological evidence that small batches of magma have pulsed into magma reservoirs is preserved in zoned crystals and melt inclusions. For example, Humphreys et al. (2006, 2008) used such evidence and other petrologic observations to suggest the magma reservoir beneath Shiveluch Volcano, Kamchatka Russia, formed slowly by the accumulation of small batches of magma. Cao et al. (2016) showed through thermomechanical modeling that multiple pulses of magma prevent a magmatic system from freezing. From thermomechanical considerations of the properties of exhumed dikes in Iceland, Gudmundsson (1984) argued that dikes form via magma pulses that are several hundred days apart. Based on thermal analysis, Menand et al. (2015) concluded that long-lived igneous bodies must grow incrementally, and they suggested continuous geodetic measurements of surface deformation could help determine whether such a body is likely to erupt. It is plausible, and we think likely, that the observed transients at Three Sisters are evidence for a magma body that is being recharged by small pulses of magma every 3–4 years and thus is growing slowly rather than freezing.

Vigneresse and Clemens (2000) suggested that magma ascent can be controlled by local or tectonic deformation and that temporal variations in deformation can lead to episodic ascent of magma. Slow-slip events occurring near Three Sisters could be such a trigger for magma-ascent transients, although the temporal correspondence is not compelling (Figure 4a). Alternatively, there is geochemical evidence for the presence of a hydrothermal system beneath South Sister (Evans et al., 2004), and if the hydrothermal system is extensive (unknown), the quasiperiodic transients could reflect recurring hydrothermal events. Such events occur below Norris Geyser Basin and elsewhere in the Yellowstone hydrothermal system (e.g., Hurwitz & Lowenstern, 2014; Lowenstern et al., 2003), for example.

Details of the inflation mechanism responsible for the TSB remain unresolved. Both ongoing magmatic intrusion at a slowly declining but variable rate and viscoelastic response of the crust to a more impulsive intrusive event in the late 1990s satisfy our observations and thus remain viable options. Viscoelastic response to a late 1990s event alone does not account for the observed spikes in inflation rate after 2000, but the spikes do not rule out this mechanism (small post-2000 intrusion events could trigger viscoelastic response). Nevertheless, we favor the simpler mechanism of persistent magma intrusion in an elastic medium. The two scenarios (intrusion with or without viscoelastic behavior) have different implications for hazards and distinguishing between them is important. In the elastic case, stresses in the crust near the source are high, as a result of a sizable and ongoing intrusion, and they will continue to increase until the intrusion stops. In the viscoelastic case, stresses are relaxing in response to a smaller intrusion that was mostly over by year 2000. The eruption potential, although small in both cases, is clearly greater in the first case. Ground deformation measurements alone are not adequate to distinguish between the alternatives, as shown by our analysis of more than two decades of such measurements. Seismic information could help to solve the puzzle, but the deforming area has produced few earthquakes so far and the area is a federally protected wilderness, which precludes tomographic studies that might be informative. Geochemical data indicate the presence of a magmatic source beneath the area (Evans et al., 2004). However, those authors surmised that the anomalies they reported probably predate the onset of the present uplift. Regardless, a magmatic source is consistent with either of the mechanisms we propose for the current episode. Repeated gravity measurements could be diagnostic, given their sensitivity to subsurface

mass changes. Zurek et al. (2012) reported results of such measurements made between 2002 and 2009. Their modeling predicted a 20–30 µGal gravity increase at the center of uplift during that period if the observed surface deformation were caused by magma intrusion. Because no significant change was detected, they concluded that viscoelastic response of the crust is the more viable uplift mechanism. However, most of the uplift occurred prior to the first gravity measurements in 2002, so the amount of mass increase during 2002–2009 (if any) would have been relatively small and, given uncertainties in measurements and modeling, might plausibly have escaped detection.

Similar inflation episodes elsewhere could easily escape detection. In this case, exploratory InSAR observations of the Three Sisters area were fortuitous, not part of a systematic monitoring program at the time. EDM and tilt-leveling networks had been established on the edifice of South Sister volcano in the early 1980s, but re-observations were sporadic, and those networks were not well situated to detect deformation centered off the edifice. The relatively minor earthquake swarm in March 2004 probably would have triggered follow-up measurements in this case, but not necessarily at more remote volcanoes elsewhere. Comprehensive, frequently repeated InSAR observations of the world's volcanoes are needed to assess the occurrence rate and hazards implications of aseismic or nearly aseismic inflation episodes. Such observations should include not only recently active volcanic edifices, but also areas of dispersed or monogenetic vents such as the central portion of the Oregon volcanic arc, which has the highest Quaternary extrusion rate along the entire arc. Our study demonstrates the utility of stacking large numbers (>100) of interferograms as a means of detecting subtle deformation signals, even if the deformation is occurring at low rates (few mm/yr) in areas with otherwise poor coherence.

The foregoing notwithstanding, episodes of noneruptive, pulsatory surface deformation attributed to intrusive activity have been recognized elsewhere, notably at Yellowstone Caldera, where alternating periods of uplift and subsidence occur both inside the caldera and along its north rim near Norris Geyser Basin (Chang et al., 2007; Dzurisin et al., 2012). Details of the inflation/deflation mechanism(s) there are a topic of ongoing research, but a continuing flux of basaltic magma to the crust, at least on geologic timescales, is unquestioned (Lowenstern & Hurwitz, 2008; Lowenstern et al., 2006). Distinguishing between such noneruptive "background" activity and other episodes of unrest that culminate in eruptions is a daunting but important research challenge, at Yellowstone but especially at many volcanoes worldwide that pose greater short-term eruptive hazards.

One aspect of that challenge is to understand better the prevalence and hazards implications of viscoelastic crustal response to magmatic intrusions. Current theory (Segall, 2010, 2016) suggests that such behavior reduces the volume of intrusion required to produce a given amount of surface deformation, for certain cases, it could be an order of magnitude or more (for example, sisO; Table 1). Such a large difference in the estimated volume of an intrusion has correspondingly large implications for the assessment of related eruptive hazards.

Intrusions ("failed eruptions") are an under-studied aspect of magmatic activity at the world's volcanoes. From a hazards perspective, distinguishing unrest that will lead to eruption from that which will not is critically important. To the extent the difference is ascertainable (the real Earth is complex and small factors might have outsized effects), the way forward is likely to include the following elements: (a) comprehensive, multidisciplinary monitoring, including space-based observations (Poland, 2015) at as many volcanoes in differing tectonic settings as possible, (b) physics-based modeling of magmatic systems (e.g., Wong & Segall, 2020); (c) geographically focused experiments at type volcanoes (e.g., Ulberg et al., 2020), and (d) a deep dive into historical records of unrest and its outcomes at volcanoes around the world (Ogburn & VDAP, 2015).

Data Availability Statement

References

Blewitt, G., Hammond, W. C., & Kreemer, C. (2009). In J. S. Oldow, & P. H. Cashman (Eds.), *Geodetic observation of contemporary deformation in the northern Walker Lane: 1. Semipermanent GPS strategy. Late cenozoic structure and evolution of the Great Basin–sierra Nevada transition* (pp. 1–15). Geological Society of America Special Paper. https://doi.org/10.1130/2009.2447(01)

Cao, W., Kaus, B. J. P., & Paterson, S. (2016). Intrusion of granitic magma into the continental crust facilitated by magma pulsing and dike-diapir interactions: Numerical simulations. *Tectonics*, *35*, 1575–1594. https://doi.org/10.1002/2015TC004076

Chang, W.-L., Smith, R. B., Wicks, C., Farrell, J. M., & Puskas, C. M. (2007). Accelerated uplift and magmatic intrusion of the Yellowstone caldera, 2004 to 2006. *Science*, *318*(5852), 952–956. https://doi.org/10.1126/science.1146842

Davis, P. M. (1986). Surface deformation due to inflation of an arbitrarily oriented triaxial ellipsoidal cavity in an elastic half-space, with reference to Kilauea Volcano, Hawaii. *J. Geophys. Res.*, *91*, 7429–7438. https://doi.org/10.1029/jb091ib07p07429

Dzurisin, D. (2021). *Results of repeated leveling surveys near the Three Sisters volcanic center, central Oregon, 2002-2008*. U.S. Geological Survey data release. https://doi.org/10.5066/P9GQ000J

Dzurisin, D., Lisowski, M., & Wicks, C. W. (2009). Continuing inflation at Three Sisters volcanic center, central Oregon Cascade Range, USA, from GPS, leveling, and InSAR observations. *Bulletin of Volcanology*, *71*(10), 1091–1110. https://doi.org/10.1007/s00445-009-0296-4

Dzurisin, D., Lisowski, M., & Wicks, C. W., Jr. (2017). Semipermanent GPS (SPGPS) as a volcano monitoring tool: Rationale, method, and applications. Journal of Volcanology and Geothermal Research. In J. Fernández, A. Pepe, M. P. Poland, & F. Sigmundsson (Eds.), *Volcano geodesy: Recent developments and future challenges* (Vol. 344, pp. 40–51). https://doi.org/10.1016/j.jvolgeores.2017.03.007

Dzurisin, D., Lisowski, M., Wicks, C. W., Jr, Poland, M. P., & Endo, E. T. (2006). Geodetic observations and modeling of magmatic inflation at the Three Sisters volcanic center, central Oregon Cascade Range, USA. *Journal of Volcanology and Geothermal Research*, *150*, 35–54. https://doi.org/10.1016/j.jvolgeores.2005.07.011

Dzurisin, D., Wicks, C. W., & Poland, M. P. (2012). History of surface displacements at the Yellowstone Caldera, Wyoming, from leveling surveys and InSAR observations, 1923–2008. *U.S. geological survey professional paper 1788, v. 1.1* (p. 68). https://doi.org/10.3133/pp1788

Ebmeier, S. K., Andrews, B. J., Araya, M. C., Arnold, D. W. D., Biggs, J., Cooper, C., et al. (2018). Synthesis of global satellite observations of magmatic and volcanic deformation: Implications for volcano monitoring & the lateral extent of magmatic domains. *Journal of Applied Volcanology*, *7*(2). https://doi.org/10.1186/s13617-018-0071-3

Evans, C. W., van Soest, M. C., Mariner, R. H., Hurwitz, S., Ingebritsen, S., Wicks, C. W., & Schmidt, M. E. (2004). Magmatic intrusion west of Three Sisters, central Oregon, USA; the perspective from spring geochemistry. *Geology*, *32*(1), 69–72. https://doi.org/10.1130/G19974.1

Gudmundsson, A. (1984). Formation of dykes, feeder-dykes, and the intrusion of dykes from magma chambers. *Bulletin of Volcanology*, *47*, 537–550. https://doi.org/10.1007/bf01961225

Guffanti, M., & Weaver, C. S. (1988). Distribution of Late Cenozoic volcanic vents in the Cascade range: Volcanic arc segmentation and regional tectonic considerations. *Journal of Geophysical Research*, *93*(B6), 6513. https://doi.org/10.1029/jb093ib06p06513

Hildreth, W., Fierstein, J., & Calvert, A. T. (2012). *Geologic map of Three Sisters Volcanic cluster, Cascade Range, Oregon: U.S geological survey scientific investigations map 3186, pamphlet 107, sheets, scale 1:24* (p. 2). https://doi.org/10.3133/sim3186

Humphreys, M. C. S., Blundy, J. D., & Sparks, R. S. J. (2006). Magma evolution and open-system processes at Shiveluch Volcano: Insights from phenocryst zoning. *Journal of Petrology*, *47*(12), 2303–2334. https://doi.org/10.1093/petrology/egl045

Humphreys, M. C. S., Blundy, J. D., & Sparks, R. S. J. (2008). Shallow-level decompression crystallisation and deep magma supply at Shiveluch Volcano. *Contributions to Mineralogy and Petrology*, *155*, 45–61.

Hurwitz, S., & Lowenstern, J. B. (2014). Dynamics of the Yellowstone hydrothermal system. *Reviews of Geophysics*, *52*(3), 375–411. https://doi.org/10.1002/2014RG000452

Iwatsubo, E. Y., Topinika, L., & Swanson, D. A. (1988). *Measurements of slope distances and zenith angles at Newberry and South Sister volcanoes, Oregon, 1985-1986* (pp. 88–377). U. S. Geological Survey Open-File Report. https://doi.org/10.3133/ofr88377

Jónsson, S., Zebker, H., Segall, P., & Amelung, F. (2002). Fault slip distribution of the 1999 Mw 7.1 Hector Mine, California, earthquake, estimated from satellite radar and GPS measurements. *Bulletin of the Seismological Society of America*, *92*(4), 1377–1389. https://doi.org/10.1785/0120000922

Langbein, J. (2004). Two-color electronic distance meter measurements revisited. *Journal of Geophysical Research*, *109*, B04406. https://doi.org/10.1029/2003JB002819

Langbein, J. (2008). Noise in GPS displacement measurements from Southern California and Southern Nevada. *Journal of Geophysical Research*, *113*. https://doi.org/10.1029/2007JB005247

Langbein, J. (2012). Estimating rate uncertainty with maximum likelihood: Differences between power-law and flicker-random-walk models. *Journal of Geodesy*, *86*(9), 775–783. https://doi.org/10.1007/s00190-012-0556-5

Lohman, R. B., & Simons, M. (2005). Some thoughts on the use of InSAR data to constrain models of surface deformation: Noise structure and data downsampling. *Geochemistry, Geophysics, Geosystems*, *6*, Q01007. https://doi.org/10.1029/2004GC000841

Lowenstern, J. B., Heasler, H., & Smith, R. B. (2003). Hydrothermal disturbances at the Norris Geyser Basin, Yellowstone National Park (USA) in 2003 (abstract). *Proceedings, fall AGU meeting*. Retrieved from https://ui.adsabs.harvard.edu/abs/2003AGUFM.V31B.05L

Lowenstern, J. B., & Hurwitz, S. (2008). Monitoring a supervolcano in repose: Heat and volatile flux at the Yellowstone caldera. *Elements, Special issue on Supervolcanoes*, *4*, 35–40. https://doi.org/10.2113/GSELEMENTS.4.1.35

Lowenstern, J. B., Smith, R. B., & Hill, D. P. (2006). Monitoring super-volcanoes—Geophysical and geochemical signals at Yellowstone and other caldera systems. *Philosophical Transactions of the Royal Society A*, *264*(1845), 2055–2072. https://doi.org/10.1098/rsta.2006.1813

Luan, F. C., & Paterson, M. S. (1992). Preparation and deformation of synthetic aggregates of quartz. *Journal of Geophysical Research*, *97*, 301–320. https://doi.org/10.1029/91jb01748

McCaffrey, R. (2009). Time-dependent inversion of three-component continuous GPS for steady and transient sources in northern Cascadia. *Geophysical Research Letters*, *36*, L07304. https://doi.org/10.1029/2008GL036784

McCaffrey, R. (2021). *TDEFNODE*. Retrieved from https://robmccaffrey.github.io/TDEFNODE/TDEFNODE.html

McCaffrey, R., King, R. W., Payne, S. J., & Lancaster, M. (2013). Active tectonics of northwestern U.S. inferred from GPS-derived surface velocities. *Journal of Geophysical Research*, *118*(2), 709–723. https://doi.org/10.1029/2012jb009473

Menand, T., Annen, C., & de Saint Blanquat, M. (2015). Rates of magma transfer in the crust: Insights into magma reservoir recharge and pluton growth. *Geology*, *43*, 199–202. https://doi.org/10.1130/G36224.1

Mogi, K. (1958). Relations between the eruptions of various volcanoes and the deformations of the ground surface around them. *Bulletin of the Earthquake Research Institute, University of Tokyo*, *36*, 99–134.

Murray, J. R., & Svarc, J. (2017). Global Positioning System data collection, processing, and analysis conducted by the U.S. Geological Survey Earthquake Hazards Program. *Seismological Research Letters*, *88*, 916–925. https://doi.org/10.1785/0220160204

Nabelek, J. (1984). *Determination of earthquake source parameters from inversion of body waves* (p. 262). Cambridge MA: Ph.D. thesisMass. Inst. of Technol.

Newman, A. V., Dixon, T. H., & Gourmelen, N. (2006). A four-dimensional viscoelastic deformation model for Long Valley Caldera, California, between 1995 and 2000. *Journal of Volcanology and Geothermal Research*, *150*(1–3), 244–269. https://doi.org/10.1016/j.jvolgeores.2005.07.017

Ogburn, S. E., & VDAP. (2015). *Eruption forecasting information system eruption chronology (EFIS echron) database. (MySQL).*

Okada, Y. (1992). Internal deformation due to shear and tensile faults in a half-space. *Bulletin of the Seismological Society of America*, *82*(2), 1018–1040. https://doi.org/10.1785/bssa0820021018

Poland, M. (2015). Volcano monitoring from space. In S. C. Loughlin, R. S. J. Sparks, S. K. Brown, S. F. Jenkins, & C. Vye-Brown (Eds.), *Global volcanic hazards and risk, chapter 17, Volcano monitoring from space* (pp. 311–316). Cambridge University Press. Retrieved from https://www.cambridge.org/core/services/aop-cambridge-core/content/view/A398156DC5B85008456DFB47882E11A0/9781316276273c17_p311-316_CBO.pdf/volcano_monitoring_from_space.pdf

Press, W. H., Flannery, B. P., Teukolsky, S. A., & Vetterling, W. T. (1989). *Numerical recipes*. Cambridge University Press.

Riddick, S. N., & Schmidt, D. A. (2011). Time-dependent changes in volcanic inflation rate near Three Sisters, Oregon, revealed by InSAR. *Geochemistry, Geophysics, Geosystems*, *12*, Q12005. https://doi.org/10.1029/2011GC003826

Rodríguez-Molina, S., González, P. J., Charco, M., Negredo, A. M., & Schmidt, D. A. (2021). Time-scales of inter-eruptive volcano uplift signals: Three Sisters volcanic center, Oregon (United States). *Frontiers in Earth Science*, *8*. https://doi.org/10.3389/feart.2020.577588

Schmalzle, G. M., McCaffrey, R., & Creager, K. C. (2014). Central Cascadia subduction zone creep. *Geochemistry, Geophysics, Geosystems*, *15*(4), 1515–1532. https://doi.org/10.1002/2013gc005172

Scott, W. E. (1987). *Holocene rhyodacite eruptions on the flanks of South Sister volcano, Oregon* (p. 18). Geological Society of America Special Paper, 212.

Segall, P. (2010). *Earthquake and Volcano deformation*. Princeton University Press. https://doi.org/10.1515/9781400833856

Segall, P. (2016). Repressurization following eruption from a magma chamber with a viscoelastic aureole. *Journal of Geophysical Research*, *121*(B12), 8501–8522. https://doi.org/10.1002/2016JB013597

Sherrod, D. R., & Smith, J. G. (1990). Quaternary extrusion rates of the Cascade Range, northwestern United States and southern British Columbia. *Journal of Geophysical Research*, *95*(B12), 19465. https://doi.org/10.1029/jb095ib12p19465

Sherrod, D. R., Taylor, E. M., Ferns, M. L., Scott, W. E., Conrey, R. M., & Smith, G. A. (2004). Geologic map of the Bend 30- 60- minute quadrangle, central Oregon. *U.S. Geological survey geologic investigations series I-2683, map plus* (p. 48). Pamphlet. https://doi.org/10.3133/i2683

Simons, M., Fialko, Y., & Rivera, L. (2002). Coseismic deformation from the 1999 M (sub w) 7.1 Hector Mine, California, earthquake as inferred from InSAR and GPS observations. *Bulletin of the Seismological Society of America*, *92*(4), 1390–1402. https://doi.org/10.1785/0120000933

Ulberg, C. W., Creager, K. C., Moran, S. C., Abers, G. A., Thelen, W. A., Levander, A., et al. (2020). Local Source Vp and Vs tomography in the Mount St. Helens region with the iMUSH broadband array. *Geochemistry, Geophysics, Geosystems*, *21*(3). https://doi.org/10.1029/2019GC008888

Vigneresse, J. L., & Clemens, J. D. (2000). Granitic magma ascent and emplacement: Neither diapirism nor neutral buoyancy. In B. Vendeville, Y. Mart, & J.-L. Vigneresse (Eds.), *Salt, shale and igneous diapirs in and around Europe* (pp. 1–19). Geological Society, London, Special Publications. https://doi.org/10.1144/gsl.sp.1999.174.01.01

Wessel, P., & Smith, W. H. F. (1998). New, improved version of the generic mapping tools released. *Eos Trans. AGU*, *79*, 579–579. https://doi.org/10.1029/98eo00426

Wicks, C. W., Jr, Dzurisin, D., Ingebritsen, S., Thatcher, W., Lu, Z., & Iverson, J. (2002). Magmatic activity beneath the quiescent Three Sisters volcanic center, central Oregon Cascade Range, USA. *Geophysical Research Letters*, *29*(7). https://doi.org/10.1029/2001GL014205

Williams, C., & Wadge, G. (1998). The effects of topography on magma chamber deformation models: Application to Mt. Etna and radar interferometry. *Geophysical Research Letters*, *25*, 1549–1552. https://doi.org/10.1029/98GL01136

Wong, Y., & Segall, P. (2020). Joint inversions of ground deformation, extrusion flux and gas emissions using physics-based models for the Mount St. Helens 2004-2008 eruption. *Geochemistry, Geophysics, Geosystems*, *21*. https://doi.org/10.1002/essoar.10504002.1

Yang, X.-M., Davis, P. M., & Dieterich, J. H. (1988). Deformation from inflation of a dipping finite prolate spheroid in an elastic half space as a model for volcanic stressing. *Journal of Geophysical Research*, *93*(B5), 4249–4257. https://doi.org/10.1029/jb093ib05p04249

Zurek, J., William-Jones, G., Johnson, D., & Eggers, A. (2012). Constraining volcanic inflation at Three Sisters Volcanic Field in Oregon, USA, through microgravity and deformation modeling. *Geochemistry, Geophysics, Geosystems*, *13*, Q10013. https://doi.org/10.1029/2012GC004341

Reference From the Supporting Information

Fu, Y., Argus, D. F., & Landerer, F. W. (2015). GPS as an independent measurement to estimate terrestrial water storage variations in Washington and Oregon. *Journal of Geophysical Research: Solid Earth*, *120*, 552–566. https://doi.org/10.1002/2014JB011415